Chemical Engineering Journal 383 (2020) 123193

Contents lists available at ScienceDirect

Chemical Engineering Journal

journal homepage: www.elsevier.com/locate/cej

# Tunable mesoporous g-$C_3N_4$ nanosheets as a metal-free catalyst for enhanced visible-light-driven photocatalytic reduction of U(VI)

Jingjing Wang[a,b,c], Yun Wang[a,b], Wei Wang[a,b], Zhe Ding[a,b], Rongyue Geng[a,b], Ping Li[a,b,*], Duoqiang Pan[c], Jianjun Liang[a,b], Haibo Qin[d], Qiaohui Fan[a,b,*]

[a] Northwest Institute of Eco-Environment and Resources, Chinese Academy of Sciences, Lanzhou 730000, China
[b] Key Laboratory of Petroleum Resources, Gansu Province, Lanzhou 730000, China
[c] School of Nuclear Science and Technology, Lanzhou University, Lanzhou 730000, China
[d] State Key Laboratory of Environmental Geochemistry, Institute of Geochemistry, Chinese Academy of Sciences, Guiyang 550081, China

## HIGHLIGHTS

- Tunable mesoporous in mpg-$C_3N_4$ improved the photocatalytic reduction for U(VI).
- mpg-$C_3N_4$ exhibited a high photocatalytic reduction efficiency to U(VI).
- The photocatalytic reduction of U(VI) was highly selective to coexisting ions.
- The photoconversion process of U(VI) was addressed using XPS, XRD and EXAFS.

## GRAPHICAL ABSTRACT

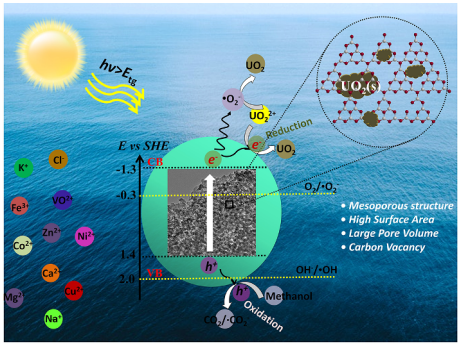


## ARTICLE INFO

*Keywords:*
Tunable mesoporous
$C_3N_4$
Photocatalysis
Uranium
Reduction

## ABSTRACT

Although photocatalytic reduction has been proven to be a green, efficient, and economical strategy for uranium (VI) extraction from water, it faces several challenges, such as low quantum conversion efficiency and utilization of sunlight. In this work, the photocatalytic efficiency of g-$C_3N_4$ was tuned by introducing proportionally-adjustable mesoporous. The prepared mesoporous g-$C_3N_4$ samples ($MCN_r$, *r* represents the initial silica/cyanamide mass ratios during synthesis) exhibited higher surface area and larger pore volume. Compared with pristine g-$C_3N_4$ (BCN), both light utilization and photo-generated carrier separation efficiency were significantly improved for $MCN_r$. $MCN_r$ showed an enhanced photocatalytic performance for the reduction of U(VI) under visible light. The optimum photocatalytic performance was achieved for $MCN_{1.0}$, which was 6.75 times higher than that of BCN. Both transmission electron microscopy (TEM) and X-ray diffraction (XRD) have confirmed the formation of $UO_2$ on $MCN_{1.0}$ surface after light irradiation. X-ray photoelectron spectroscopy (XPS) and extended X-ray absorption fine structure (EXAFS) further revealed the re-oxidation of $UO_2$ during the photocatalytic process. A high uranium extraction capacity (~2990 mg/g) could be achieved by $MCN_{1.0}$, and the deposited $UO_2$ could be easily eluted by 0.01 mol/L $Na_2CO_3$ solution after exposure to air, showing high reuse performance. In the presence of co-existing ions, the photocatalytic reduction of U(VI) remained a high selectivity.

* Corresponding authors at: Northwest Institute of Eco-Environment and Resources, Chinese Academy of Sciences, Lanzhou 730000, China.
*E-mail addresses:* liping@lzb.ac.cn (P. Li), fanqh@lzb.ac.cn (Q. Fan).

https://doi.org/10.1016/j.cej.2019.123193
Received 1 July 2019; Received in revised form 25 September 2019; Accepted 14 October 2019
Available online 15 October 2019
1385-8947/ © 2019 Elsevier B.V. All rights reserved.

## 1. Introduction

As the fast development of nuclear energy, the uranium resource has become increasingly crucial to the nuclear industry [1]. However, the terrestrial supply of uranium is limited, which was reported to be depleted in one century [1,2]. As a result, seawater uranium extraction has attracted extensive attention for a long time, owing to the large content of uranium in seawater (~4.5 billion tons), which is approximately a thousand times greater than terrestrial uranium resources [3]. In the past 50 years, adsorption strategy has been widely used for uranium extraction from seawater, mostly using functionalized polymer fibers as sorbents [4–11]. However, the extraction of uranium from seawater via physicochemical adsorption is significantly challenging, mainly owing to the extremely low U(VI) concentrations (~3.0 ppb) and the abundant coexisting metal ions (e.g., $Na^+$, $K^+$, $Mg^{2+}$, $Ca^{2+}$, $Cu^{2+}$, $Fe^{3+}$, $VO_2^+$) [1,11]. Moreover, the elution conditions for captured U(VI) and V(V) are generally harsh enough to destroy the sorbents, making the sorbents hard to be reused [12]. Thus, there is an urgent need to develop new strategies for seawater uranium extraction.

Our previous work showed that efficient seawater uranium extraction could be achieved by applying a photocatalysis method [13,14], where U(VI) was reduced to U(IV), existing in the form of $UO_2$ nanoparticles on $TiO_2$ surface. Compared with physicochemical adsorption, the photocatalysis method has higher efficiency and selectivity [15–19], and has been proven to be a non-polluting, economical, and facile method for U(VI) extraction [13,20–25]. Despite the remarkable advantages, proper photocatalysts are required for this technique. To date, $TiO_2$ has been mostly applied in the photocatalytic U(VI) reduction, where UV irradiation was necessary due to the wide bandgap of $TiO_2$ (3.2 eV). However, UV light only occupies about 4% of solar energy, which seriously inhibits the photocatalytic efficiency and practical applications [26].

In the past decade, metal-free graphitic carbon nitride (g-$C_3N_4$) has attracted extensive attentions owing to its low cost, high stability, relative facile synthesis, and moderate energy gap (~2.7 eV) [27]. These unique properties enable g-$C_3N_4$ to be widely used for visible light photocatalytic applications such as water splitting, $CO_2$ reduction, organics photodegradation, and fuel cells [28–35]. The conduction band (CB) position of g-$C_3N_4$ is −1.23 V (vs. SHE at pH 7.0), which is more negative than the reduction potential of $UO_2^{2+}/U^{4+}$ (0.267 V) and $UO_2^{2+}/UO_2$ (0.411 V) [24,25]. Accordingly, the photocatalytic U(VI) reduction is thermodynamically feasible. However, bulk g-$C_3N_4$ (BCN) obtained through the direct thermal polymerization process generally yields relatively low specific areas and less active sites, which leads to poor performance in catalytic processes [33]. In addition, the quantum efficiency of BCN in the visible light region needs further improvement. It has been shown that the electronic band structures of g-$C_3N_4$ could be tuned by the modification of morphology [36]. The fabrication of mesoporous-structured g-$C_3N_4$ is an effective method to promote the photocatalytic performance of g-$C_3N_4$ without introducing any impurity [37,38]. Compared with bulk samples, porous g-$C_3N_4$ has a higher specific surface area and accessible porosity, which can provide more active chemical sites for photocatalytic reactions as well as higher size- or shape-selectivity [39]. This can be attributed to the fact that mesoporous structures can enhance light utilization through increasing light scattering and refraction processes in the pore channels [38,40,41].

Considering the excellent physicochemical and optical properties of mesoporous g-$C_3N_4$, it is expected to be a good candidate to efficiently extract U(VI) from water. Therefore, mesoporous g-$C_3N_4$ ($MCN_r$) samples with different amounts of pores were fabricated and characterized in this study. The photocatalytic performance and mechanism of U(VI) reduction over the synthesized samples were evaluated and addressed in detail combining spectroscopic approaches. The results will serve to enhance understanding of the photocatalytic reduction of U(VI), and are promising to promote the potential application of the photocatalytic method under visible light.

## 2. Experimental section

### 2.1. Photocatalysts preparation

Scheme 1 illustrates the synthesization of mpg-$C_3N_4$ with the hard template method [41]. Briefly, 1.0 g of cyanamide (99%) was stirred at 70 °C, and different amounts (0.625, 1.25, 2.5, 5.0, and 10 g, respectively) of 40% dispersion of $SiO_2$ particles with a size of 12 nm (Ludox HS40, Aldrich) were added dropwise. The mixtures were heated overnight at 70 °C with stirring to evaporate water. Afterwards, the dried sample was thermally treated at 550 °C for 4 h in a tube furnace under $N_2$ atmosphere, where the heating rate was 2 °C/min. Subsequently, the reactor was spontaneously cooled to 25 °C. The resulting yellow powders were treated with 4.0 mol/L $NH_4HF_2$ for 24 h to remove the $SiO_2$ template, and then was washed with distilled water and ethanol for several times. Finally, the powders were dried with a vacuum freeze dryer. The as-prepared samples were labeled as $MCN_r$ ($r$ refers to the initial silica/cyanamide mass ratios of 0.25, 0.5, 1.0, 2.0 and 4.0, respectively). For comparison, a bulk g-$C_3N_4$ sample (labeled as BCN) was synthesized by directly heating 1.0 g of cyanamide in the tube furnace at 550 °C.

### 2.2. Characterization

Morphology and structures were characterized with transmission electron microscopy (TEM, Fei Tecnai G2 F30) and X-ray diffraction (XRD) (D/Max-2400, Rigaku, Japan) instrument equipped with Cu Kα, respectively. Fourier-transform infrared (FT-IR) spectra were obtained on a Bruker Alpha instrument, and the spectra were average over 120 scans with a spectral resolution of 4 $cm^{-1}$. The Brunauer-Emmett-Teller (BET) area was measured by Tristar II 3020, and degassing was performed at 100 °C before detection. Pore-size distributions were calculated with the Barrett–Joyner–Halenda (BJH) method. The surface chemical component and oxidation states were characterized using X-ray photoelectron spectroscopy (XPS) (Kratos AXIS Ultra$^{DLD}$) with Al-Kα radiation at 10 kV and 5 mA. The binding energies of XPS spectra were referenced by C 1 s at 284.6 eV. UV–vis diffuse reflection spectrum (DRS) was gained using Kubelka-Munk function ($F(R_\infty) = (1-R_\infty)^2/(2R_\infty)$) by UV–vis spectrophotometer (UV-2550, Shimadzu, Japan),

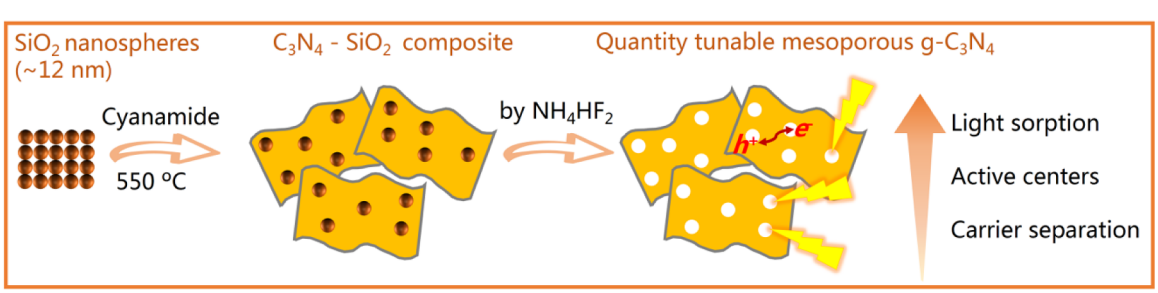


**Scheme 1.** Schematic diagram for the preparation of $MCN_r$ samples.

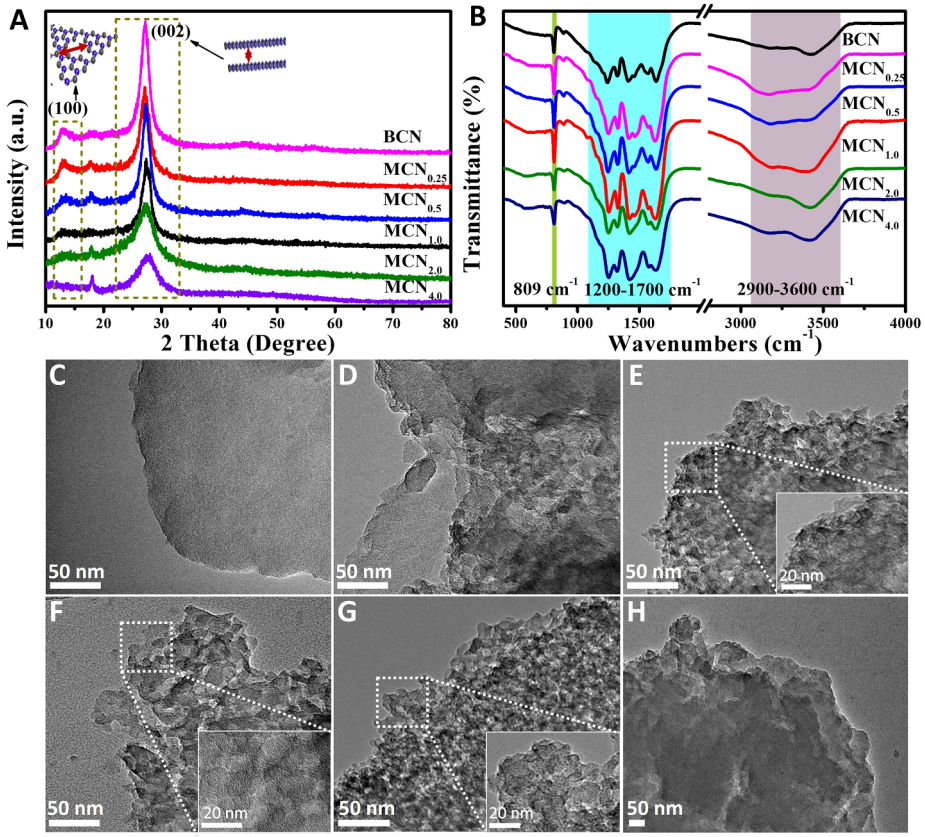


**Fig. 1.** XRD patterns (A); FT-IR spectra (B); TEM images for BCN (C), $MCN_{0.25}$ (D), $MCN_{0.5}$ (E), $MCN_{1.0}$ (F), $MCN_{2.0}$ (G), and $MCN_{4.0}$ (H).

where $R_\infty$ was the reflectance of samples. According to the equation: $(\alpha h\upsilon)^{1/2} \propto h\upsilon - Eg$, the bandgap energy (Eg) was obtained by extrapolating the linear portion of the plots between $(\alpha h\nu)^{1/2}$ against $h\nu$ to Y-axis = 0, where α was the absorption coefficient, $\nu$ is the frequency, and $h$ is Planck's constant [42]. Photoluminescence (PL) spectra and the photoluminescence emission lifetimes were obtained through a fluorescence spectrophotometer (FLS920, Edinburgh Instrument, UK) at room temperature. The electron spin resonance (ESR) measurement was carried out on Bruker A300 spectrometer under visible light irradiation (λ > 420 nm), where 5,5-dimethyl-l-pyrroline N-oxide (DMPO) was used as a probe.

Uranium $L_{III}$-edge X-ray absorption near edge structure (XANES) and extended X-ray absorption fine structure (EXAFS) were collected at the beamline BL14W1 station of Shanghai Synchrotron Radiation Facility (SSRF, China). The electron beam energy and average stored current were 3.5 GeV and 220 mA, respectively. During the measurements, the double-crystal Si (1 1 1) monochromator was slightly detuned to reduce the high-order harmonics and to control the total fluorescence counts. XANES and EXAFS were collected under fluorescence mode with a Lytle detector [43]. The EXAFS data were analyzed using Athena and Artemis interfaces compacted in IFFEFIT [44] and FEFF 7.0 [45].

### 2.3. Photoelectric chemistry experiments

The photocurrent was measured on a CHI 660D electrochemical workstation (Shanghai Chenhua, China) in a typical three-electrode potentiostat system. Briefly, 0.7 mg photocatalyst and 0.3 mg graphitized carbon black were added into a 0.95 mL ethyl alcohol and 50 μL Nafion solution. The formed slurry was then dip-coated onto the L-type glassy carbon electrode, which was used as the working electrode after drying at 40 °C for 30 min. A Pt sheet and standard Ag/AgCl (in saturated KCl) were used as the counter electrode and reference electrode, respectively. For the electrolyte, 0.1 mol/L of $Na_2SO_4$ aqueous solution was used. The variations of photoinduced current density with time (*i–t* curve) were measured using a Xe lamp (300 W) with a UV-cutoff filter as the light resource (λ > 420 nm).

### 2.4. Photocatalysis tests

In the catalytic process, 75 mg $MCN_r$ was added into 15 mL $1.0 \times 10^{-4}$ mol/L $UO_2^{2+}$ solution (containing 2.5 mL methanol as the electron sacrifice). The pH value was adjusted to 6.0 with a negligible volume of HCl and/or NaOH solution. The visible light irradiation was obtained from a 300 W Xe lamp equipped with a 420 nm cutoff filter. Before irradiation, the reaction system was bubbled with argon in dark for 2 h to maintain anaerobic conditions and reach the adsorption–desorption equilibrium. After irradiation, 1 mL of suspension was pipetted out at a certain time and rapidly filtered using a 0.22 μm membrane. U(VI) concentration was measured by UV–vis spectrophotometry at 652 nm using Arsenazo III (The detection limit for uranium is lower than $1.0 \times 10^{-7}$ mol/L) and inductively coupled plasma optical emission spectrometry (ICP-OES, the detection limit for uranium was ~100 ppb). $UO_2^{2+}$ solution without photocatalysts was also irradiated under the above conditions for comparison. The concentrations of metal ions (Cu, Fe, V, Mg, Ca, Na, K, and Zn) were detected by ICP-OES. In the quenching experiments, tertiary butanol (TBA), p-benzoquinone (P-BQ) and methanol were added as scavengers for $^{\cdot}OH$ radicals, $O_2^{\cdot -}$ radicals, and holes, respectively [22].

## 3. Results and discussion

### 3.1. Characterization

The structures of the as-prepared $MCN_r$ ($MCN_{0.25}$, $MCN_{0.5}$, $MCN_{1.0}$, $MCN_{2.0}$, and $MCN_{4.0}$) and BCN samples were studied by XRD as shown

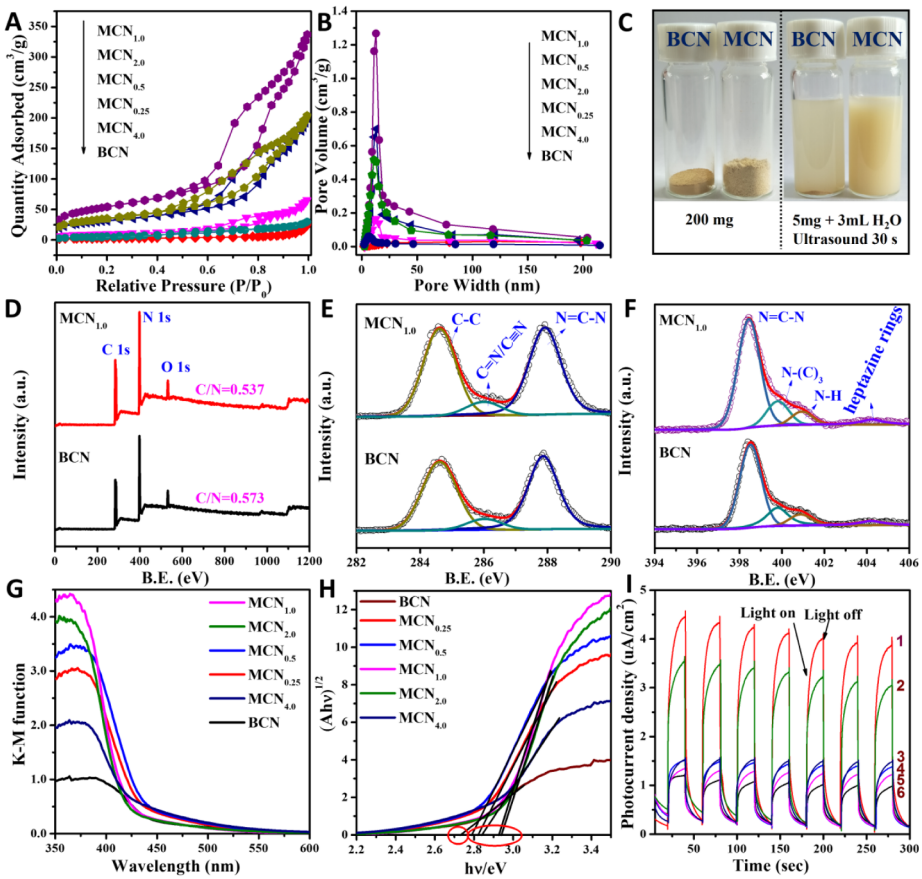


**Fig. 2.** $N_2$ adsorption-desorption isotherms at 100 °C (A); The corresponding PSD curves (B); Photograph of 200 mg powder and dispersion in water (C); XPS spectra of BCN and $MCN_{1.0}$ (D); The corresponding high-resolution C1s spectra (E) and N1s spectra (F); UV–vis DRS of BCN and $MCN_r$ photocatalysts (G); Plot of $(Ah\nu)^{1/2}$ versus photon energy (eV) (H); *I-t* spectra of as-synthesized BCN and $MCN_r$ samples (1: $MCN_{1.0}$; 2: $MCN_{2.0}$; 3: $MCN_{4.0}$; 4: $MCN_{0.5}$; 5: $MCN_{0.25}$; and 6: BCN) (I).

in Fig. 1A. For both $MCN_r$ and BCN, the peaks at 13.1° (assigned to (1 0 0) faces), 17.8° (assigned to (6 0 0) faces), and 27.4° (assigned to (0 0 2) faces) were observed in the XRD pattern, which can be ascribed to the in-plane structural packing of tri-s-triazine motifs, the denser packing or a distortion of the melon structure, as well as the inter-layer stacking of conjugated aromatic systems, respectively [24,46]. Nevertheless, peak broadening related to the (0 0 2) faces and a decrease in the overall peak intensity were observed for $MCN_{2.0}$ and $MCN_{4.0}$, implying lower crystallinity. Such phenomena are possibly due to (1) incomplete polymerization and structural defects, reflecting the effect of geometric confinement in the nanosized pore channel [41]; and (2) the formation of small g-$C_3N_4$ pieces when excess templates was used. The functional groups on $MCN_r$ were characterized by FT-IR, as shown in Fig. 1B. The broad absorption band at ~2900–3600 $cm^{-1}$ could be ascribed to the stretching vibration modes for the N–H and hydroxyl groups of adsorbed $H_2O$. The peaks in the range from 1200 to 1700 $cm^{-1}$ represent the stretching modes of aromatic $C_3N_4$ heterocycles, while the peak at ~809 $cm^{-1}$ could be attributed to the typical breathing mode of the triazine units [47]. All the $MCN_r$ samples ($MCN_{0.25}$, $MCN_{0.5}$, $MCN_{1.0}$, $MCN_{2.0}$, and $MCN_{4.0}$) exhibited characteristics similar to BCN, which suggests a similar chemical structure. It is noteworthy that the intensity of the band at 2900–3600 $cm^{-1}$ of the $MCN_r$ samples is quite strong in contrast to BCN, especially in $MCN_{1.0}$. The result implies the existence of the porous, which could adsorb a larger amount of $H_2O$ than the bulk one [37].

Fig. 1C–H and Fig. S1 (in Supplementary Information, SI) show the morphology and microstructure of BCN and $MCN_r$. It is clear that all samples were laminar. Compared with BCN, wormhole-like mesostructures without long-range order could be observed on $MCN_r$. For $MCN_{0.25}$, few wormhole structures were disorderly distributed on the bulk surface. As the template amount increased, more wormhole-like mesostructures appeared and were uniformly distributed. However, the mesoporous structure were almost destroyed when the mass ratio of templates to cyanamide increased to 4.0 ($MCN_{4.0}$), and an amount of small-sized plates were observed to stack together. This was considered that, with the large amount of templates, the in-plane structural packing of tri-s-triazine motifs was interrupted to some extent. It was also supported by the XRD patterns (Fig. 1A), where the intensity of (1 0 0) faces significantly decreased. In the case of $MCN_{4.0}$, the BCN layers were completely "cut" into small and irregular pieces by templates (20–30 nm, Fig. S2). These pieces clustered together, followed by the increase to some extent in the thickness (Fig. 1H) [37,41]. The formation of small pieces of $MCN_{4.0}$ further supported the observation of the broaden (0 0 2) peaks in the XRD patterns.

Fig. 2A displays the nitrogen adsorption-desorption isotherms of the $MCN_r$ and BCN. In the case of pristine BCN, a weak $N_2$ adsorption possibly suggested the nonporous structure. While all $MCN_r$ samples demonstrated the type-IV isotherms bearing H1-type hysteresis loops, indicating mesoporous characteristics of the prepared photocatalysts [47]. To further analyze the pore structures of $MCN_r$ samples, the pore size distributions (PSD) were calculated using the BJH method from the desorption branch of the nitrogen isotherms (Fig. 2B). The pristine g-$C_3N_4$ showed negligible pores, and the average pore sizes were uniformly near 12 nm for the $MCN_{0.25}$, $MCN_{0.5}$, and $MCN_{1.0}$ samples, which could be regarded as a replica of the structure of the silica spheres (~12 nm, see Fig. S1A). However, for $MCN_{2.0}$ and $MCN_{4.0}$, a significant decrease in the number of pores was demonstrated. The small pore size further confirmed the speculation that stackable small $C_3N_4$ pieces could be formed when the content of templates was high.

BET specific surface area (SSA), pore size, and average pore volume are listed in Table 1. Compared with BCN (9 $m^2/g$), the SSA of $MCN_r$ were significantly improved (23–191 $m^2/g$), depending on the content of template. $MCN_{1.0}$ had the largest surface area among all the as-prepared samples. $MCN_{0.25}$ and $MCN_{0.5}$ possessed fewer holes

**Table 1**
The structure parameters of BCN and $MCN_r$ samples.

| sample | BET surface area ($m^2/g$) | Total pore volume ($cm^3/g$) | Average pore diameter (nm) | Band-gap (eV) |
|---|---|---|---|---|
| BCN | 9.1 ± 0.8 | 0.04 | 17.6 | 2.73 |
| $MCN_{0.25}$ | 34.1 ± 1.1 | 0.10 | 11.9 | 2.81 |
| $MCN_{0.5}$ | 111.0 ± 7.1 | 0.31 | 11.1 | 2.79 |
| $MCN_{1.0}$ | 190.7 ± 10.0 | 0.52 | 10.9 | 2.92 |
| $MCN_{2.0}$ | 124.5 ± 6.2 | 0.32 | 10.1 | 2.94 |
| $MCN_{4.0}$ | 23.0 ± 2.5 | 0.05 | 7.5 | 2.84 |

compared with $MCN_{1.0}$, owing to the lower content of template. In the cases of $MCN_{2.0}$ and $MCN_{4.0}$, the limited pores resulted in smaller SSA. The SSA and total pore volume of $MCN_{1.0}$ were ~191 $m^2/g$ and ~0.52 $cm^3/g$, respectively, which were 21.8 and 13.0 fold higher than that of BCN, respectively (Table 1). Compared with BCN, the high SSA and large pore volume for $MCN_{1.0}$ resulted in a much larger volume and better water dispersibility (Fig. 2C) [47].

To further explore the surface species and elemental valence states in $MCN_r$ samples, the XPS measurements were conducted. As shown in Fig. 2D, XPS spectrum of $MCN_{1.0}$ mainly consisted of three sharp peaks at 287.3, 398.3, and 531.3 eV, which were ascribed to C 1 s, N 1 s, and O 1 s signals, respectively. The O 1 s signal may be due to the surface absorbed $CO_2$ and $H_2O$ [47]. To gain insight into the chemical bonding between C and N atoms, high-resolution spectra of C 1 s and N 1 s were analyzed, respectively (Fig. 2E and F). For $MCN_{1.0}$, the C 1 s spectrum was composed of $sp^2$ C−C, C=N/C≡N (from the defect-containing $sp^2$-hybridized carbon atoms), and N=C−N bonds at 284.6 eV, 286.0 eV, and 288.0 eV, respectively (Fig. 2E). The N 1 s spectrum (Fig. 2F) was deconvoluted into N=C−N (~398.5 eV), N−$(C)_3$ (~399.8 eV), N−H (~400.8 eV), and C−N−H (~404.3 eV, from the positive charge localization in heptazine rings due to incomplete condensation), respectively [48]. In addition, it was noted that the surface C/N atomic ratio of $MCN_{1.0}$ (0.57) slightly decreased relative to BCN (0.53), which may be attributed to uncondensed amino functions [41]. Therefore, it was speculated that the structural defects can selectively create more carbon vacancies (CVs), which are also expected to improve the photocatalytic activity of g-$C_3N_4$ [49].

The optical absorption properties of BCN and $MCN_r$ were also measured by UV/vis DRS. As shown in Fig. 2G, all samples demonstrated a typical semiconductor absorption pattern in the visible range. Compared to BCN, an upshift in light absorbance in the region of 400–600 nm was observed for all $MCN_r$ samples. The enhanced light-trapping effect was attributed to multiple reflection or transmission of light scattered by the pore walls in the $MCN_r$ body [38]. The high visible light absorbance indicates that the obtained $MCN_r$ samples have higher visible light utilization efficiency, which is conducive to enhance the photoactivity. In addition, an increase in the band gap energy was observed for $MCN_r$ (Fig. 2H and Table 1), which was caused by the quantum confinement effect with the CB and VB shifting in opposite directions [38,47,50].

The photocurrent-time measurement in on-off cycles was employed to evaluate the photo-carriers separation dynamics of BCN and $MCN_r$ electrodes under visible light irradiation. Compared with BCN, $MCN_r$ photocatalysts displayed much higher photocurrent intensity following in the sequence of $MCN_{1.0}$ > $MCN_{2.0}$ > $MCN_{4.0}$ > $MCN_{0.5}$ > $MCN_{0.25}$ > BCN (Fig. 2I). Obviously, both the largely increased specific surface area and abundant pore walls lead to the enhancement of visible light absorption, although the bandgap was increased for $MCN_r$. The results further indicated that the introduction of mesoporous played a critical role in charge separation and the increased visible light absorption. The photocurrent intensity generated by the $MCN_{1.0}$ electrode was the highest (4.11 μA $cm^{-2}$), which was 4.0 times of that induced by BCN (1.03 μA $cm^{-2}$). As a result, $MCN_{1.0}$ exhibited the highest efficiency in separating photo-generated charge carriers [51].

### 3.2. Photocatalytic activity under visible light

The photocatalytic activities of BCN and $MCN_r$ for U(VI) reduction are shown in Fig. 3A. In the dark, the adsorption of U(VI) on $MCN_r$ was chemical and monolayer process (Fig. S4 and S5). The adsorption of U(VI) on $MCN_r$ increased with increase in $r$ from 0.25 to 4.0, which was mainly owing to the increase of the adsorption sites at the edge of pores and g-$C_3N_4$ plates. When the systems were irradiated under visible light, the residual U(VI) in the solutions decreased rapidly. For comparison, the solution without photocatalysts was illuminated under visible light for 40 min, and no significant decline of U(VI) concentration was observed, suggesting that self-photolysis of $UO_2^{2+}$ was negligible. The photocatalytic activity followed the sequence of $MCN_{1.0}$ > $MCN_{2.0}$ > $MCN_{0.5}$ > $MCN_{0.25}$ > BCN. By applying the pseudo-first-order reaction ($-\ln(C/C_0) = kt$) (where $k$ is the reaction rate constant ($min^{-1}$) of U(VI), and $C_0$ and $C$ are the concentrations of U(VI) (mol/L) corresponding to 0 and $t$ min, respectively) [52], the corresponding rate constants ($k$) were deduced as 0.27 ($MCN_{1.0}$), 0.15 ($MCN_{2.0}$), 0.08 ($MCN_{0.5}$), 0.06 ($MCN_{0.25}$) and 0.04 (BCN) $min^{-1}$, respectively (Fig. 3B). The photocatalytic efficiency of $MCN_{1.0}$ was 6.75 times higher than that of BCN and 100% U(VI) conversion was achieved within 20 min, exhibiting the best performance for uranium extraction. Moreover, the performance of U(VI) reduction over $MCN_{4.0}$ was also compared with that of $MCN_{1.0}$ at a higher initial U(VI) concentration ($2.0 \times 10^{-4}$ mol/L) (Fig. S7). $MCN_{1.0}$ exhibited much higher efficiency for photocatalytic U(VI) reduction than $MCN_{4.0}$ did (Fig. S7). Due to the largest SSA, the most abundant nanoscale pore walls, and appropriate defects, $MCN_{1.0}$ could achieve optimal surface mass transfer, offering more plentiful active centers and exhibiting the highest visible-light utilization efficiency. Fig. S8 compared the performance difference for the U(VI) reduction between $MCN_r$ and reported catalysts. Compared with other photocatalysts, under the studied conditions, $MCN_{1.0}$ hold the optimum photocatalytic efficiency for U(VI) reduction.

Fig. 3C shows the PL spectra with an excitation wavelength of 354 nm. The luminescence was observed over a wide range (400 – 700 nm) for the $MCN_{1.0}$ and BCN samples, and both exhibited a maximum at approximately 470 nm, which was the characteristic band-band PL phenomenon from the n-π* electronic transitions for g-$C_3N_4$ [25]. Clearly, $MCN_{1.0}$ showed lower PL intensity than that of pristine BCN, indicating electron localization on the surface terminal sites [38]. In other words, the recombination probability of charge carriers in the $MCN_{1.0}$ was lower. As a result, $MCN_{1.0}$ showed higher photocatalytic activity than BCN did, suggesting that the introduction of pore on BCN enhanced the separation and transport efficiency of photo-generated electron-hole ($e^-$-$h^+$) pairs, which is crucial for improving the photocatalytic reaction. To further understand the recombination kinetics of photoinduced charge, the time-resolved PL spectra of BCN and $MCN_{1.0}$ were recorded (Fig. 3D). The average PL lifetime (τ) was deduced as:

$$\tau = \frac{A_1\tau_1^2 + A_2\tau_2^2 + A_3\tau_3^2\cdots}{A_1\tau_1 + A_2\tau_2 + A_3\tau_3\cdots} \quad (1)$$

Fitting the decay spectrum revealed three radiative lifetimes with different percentages as given in the inset in Fig. 3D. Specifically, the average PL lifetime of $MCN_{1.0}$ (59 ns) was 1.6 times longer than that of BCN (37 ns). In detail, the percentage of charge carriers with a lifetime shorter than 4 ns decreased from 73.04% for BCN to 66.75% for $MCN_{1.0}$. Meanwhile, the longest lifetime increased from 69.52 ns in BCN to 97.24 ns in $MCN_{1.0}$, and the percentage rose by 0.59%. The longer intrinsic fluorescence lifetime is also expected to improve the transport rate of photocarriers in the $MCN_r$ samples [53]. In summary, the above results indicate that $MCN_r$ exhibited a significantly improved photocatalytic performance for the reduction of U(VI), owing to higher

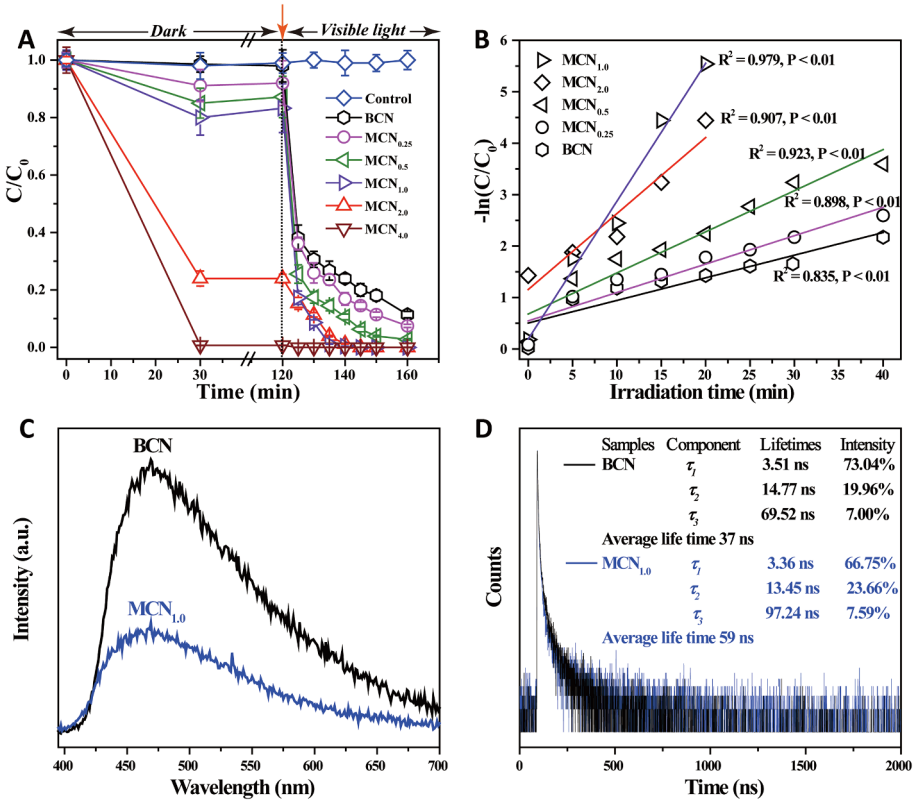


**Fig. 3.** The variation of $UO_2^{2+}$ concentration vs. illumination time with BCN and $MCN_r$, $C(UO_2^{2+}) = 1.0 \times 10^{-4}$ mol/L, $s/l = 0.5$ g/L, pH = 6.0 (A), (Control group: U(VI) was illuminated in the absence of photocatalyst); The corresponding pseudo-first-order rate constant of $UO_2^{2+}$ reduction (B); PL spectra of BCN and $MCN_{1.0}$ under 375 nm excitation (C); Time-resolved PL spectra monitored under 375 nm excitation for BCN (black) and $MCN_{1.0}$ (blue) (D). (For interpretation of the references to color in this figure legend, the reader is referred to the web version of this article.)

surface area, increased light absorption, and reasonable structural defects. However, when excess amount of templates were applied, the photocatalytic U(VI) reduction was restrained due to the destroy of the mesoporous structures.

### 3.3. Practical application

As shown in Fig. 4A, 73% of the 0.01 mol/L U(VI) could be extracted by photoreduction on $MCN_{1.0}$ within 1 h, and the extraction capacity of uranium reached 2.77 g of U per g-photocatalyst. This high extraction capacity by photocatalytic method was significantly higher than the reported results of physicochemical adsorption and electrochemical methods [1,5–9,54]. The photoreduction method was also investigated using U(VI)-spiked real seawater (from the Bohai Sea, (118°05′46″, 38°48′02″)) to demonstrate its realistic application. As can be seen from Fig. 4B, in the dark, the adsorption of U(VI) was higher than that in pure water owing to higher pH (~8.02) of the seawater. Under visible light irradiation, the kinetic uranium extraction in the seawater was similar to that in pure water, and all U(VI) was extracted within 20 min, indicating a high photoreduction efficiency in a real seawater system.

To evaluate the influence of competing ions (e.g., $VO_2^+$, $Fe^{3+}$, $Na^+$, $K^+$, $Cu^{2+}$, $Zn^{2+}$, $Ca^{2+}$, and $Mg^{2+}$), the photocatalytic reduction of U (VI) was tested in the presence of the above ions with the same concentration as U(VI) (Fig. 4C). In the dark, the adsorption of U(VI) was negligibly changed in the presence of the coexisting metal ions. For the competing ions, $Na^+$, $K^+$, $Zn^{2+}$, $Ca^{2+}$, and $Mg^{2+}$ were almost not adsorbed, while the adsorption of $Cu^{2+}$, $Fe^{3+}$, and $VO_2^+$ was 53%, 95%, and 24%, respectively. The different adsorption of coexisting cations is mainly related to their differing valency, radii, softness, and hydrolysis abilities [55]. After 1 h irradiation, 84.5% of U(VI) was extracted while the extraction efficiency of $Cu^{2+}$ and $VO_2^+$ was 99% and 94%, respectively. However, after irradiation, the removal of Fe significantly declined from 95% to 2.8%. To explore the reaction mechanisms, the valence states of Cu, Fe and V were determined by XPS (Fig. S9). It was confirmed that the binding energy (B.E.) of Cu 2p and Fe 2p shifted lower after irradiation, indicating the photoreduction of Cu(II) and Fe(III) (Figs. S9A and S9D). Combined with Auger Cu LMM spectrum (Fig. S9B), the formation of $Cu_2O$ at the surface of $MCN_{1.0}$ has been confirmed, which resulted in the increased removal of Cu(II) after irradiation. On the contrary, the reduction of Fe(III) to Fe(II) would surely decrease the adsorption affinity of iron ions with the $MCN_{1.0}$ surface. For V, the B.E. of V 2p did not change after irradiation, which indicated that the redox reaction did not occur during irradiation in the case of $VO_2^+$. Therefore, the increased removal of V after irradiation might be in terms of the desorption of $Fe^{3+}$. During irradiation, the accumulation of Fe(III) on $MCN_{1.0}$ surface significantly decreased and released the active sites that were bounded by $VO_2^+$. Overall, in the presence of abundant co-existing ions, despite the deposition of $Cu_2O$ and increased adsorption of V, a relatively high efficiency was still retained for uranium extraction.

The elution of uranium is also crucial to the recovery of uranium and the reuse of photocatalyst. In physicochemical adsorption, uranyl ions adsorbed onto amidoxime polymers should be eluted by strong acidic solution. The elution conditions are generally harsh enough to destroy the sorbent or damage the active sorption sites irreversibly, making the reuse of the sorbents difficult [12]. For the electrochemical method, both HCl and reverse bias were required to recover 96.2% of the extracted uranium [1]. In the present study, after the uranium was photo-deposited, the catalyst was collected and re-dispersed in deionized water. By simply exposing to air, 45% of uranyl ions can be directly recovered, derived from the re-oxidation of reduced uranium in air (Fig. 4D). Thereafter, when 0.1 M $Na_2CO_3$ solution was added, 100% U(VI) was recovered (Fig. 4D). This process was efficient, non-polluting, and much easier compared with the physicochemical adsorption and electrochemical methods [1,13]. Finally, using the photodeposition-stripping methods, five successive circulating runs were executed to assess the reusability of mesoporous g-$C_3N_4$. As shown in Fig. 4E, there was no significant decline in the photocatalytic activity after five recycles, indicating that $MCN_{1.0}$ could maintain stable during the

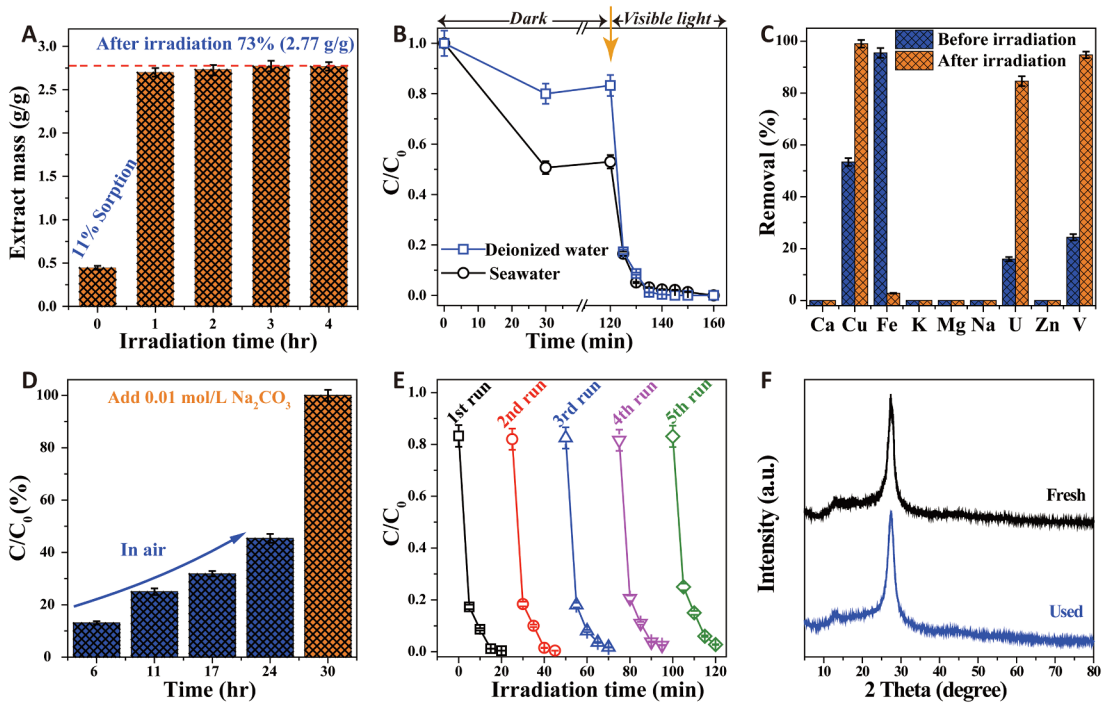


**Fig. 4.** Uranium extraction performance using photocatalytic method. $C(UO_2^{2+}) = 0.01$ mol/L, pH = 6.0, $s/l = 0.6$ g/L (A); U(VI) removal in deionized and spiked real sea water. $C(UO_2^{2+}) = 1.0 \times 10^{-4}$ mol/L, pH = 6.0, $s/l = 0.5$ g/L (B); Removal of metal ions with $MCN_{1.0}$ before and after irradiation under visible light for 1 h. $C$(metal ions) = $1.0 \times 10^{-4}$ mol/L, pH = 6.0, $s/l = 0.5$ g/L (C); The elution of photo-induced uranium deposits (D); Cycling runs for the photocatalytic reduction of $UO_2^{2+}$ over $MCN_{1.0}$ sample under visible light irradiation (E); XRD patterns before and after irradiation (F). $C(UO_2^{2+}) = 1.0 \times 10^{-4}$ mol/L, pH = 6.0, $s/l = 0.5$ g/L.

photocatalytic reactions. This was further supported by the XRD and FT-IR investigations, where no distinct alteration was observed for structure and functional groups on $MCN_{1.0}$ after irradiation (Fig. 4F and Fig. S10A). The mesoporosity of $MCN_{1.0}$ was also well maintained after five cycle tests (Fig. S10B). The above results proved that the $MCN_{1.0}$ catalyst exhibits high efficiency, appropriate selectivity, good stability and reusability for the photocatalytic removal of U(VI) and is promising for practical application in uranium extraction from aqueous solution.

### 3.4. Photocatalytic reduction mechanism

Although it has been widely accepted that U(VI) was photoreduced to U(IV), the transformation process still remains controversial, meriting further research. As shown in Fig. S11, the color of U(VI)-adsorbed $MCN_{1.0}$ is yellow, which turned to gray under light irradiation. Salomone et al. [52] demonstrated that the dark gray precipitation formed by $TiO_2$-induced photoreduction was $UO_{2+x}$ (x = 0–0.25). Similarly, Amadelli et al. [56] reported uranyl oxide photodeposited on $TiO_2$ powder with a stoichiometry close to $U_3O_8$ by infrared analyses. In addition, Lee et al. [3] observed three lower oxidation states (i.e., $U^{4+}$, $U^{14/3+}$, and $U^{16/3+}$) in the production on semiconductor electrodes. XPS identified the major ionic species after photoelectrochemistry treatment as $U^{6+}$, $U^{4.6+}$, and $U^{4+}$ [57]. Meanwhile, other studies confirmed the copresence of both U(VI) and U(IV) after photoreduction [24,25,58].

Fig. 5A shows the XRD patterns of $MCN_{1.0}$ before and after U(VI) photoreduction. One can see that for U(VI)-adsorbed $MCN_{1.0}$, no new peak was observed, except for the characteristic peaks from $MCN_{1.0}$ (~13.1° and 27.4°). However, the typical peaks of $UO_2$ located at ~28.1°, 32.4°, 46.8° and 55.9° were observed after visible light irradiation, indicating that the conversion of U(VI) to $UO_2$(s), which is similar to the results in Li et al. [13]. It was also very interesting to note that meta-schoepite ($(UO_2)_8O_2(OH)_{12}(H_2O)_{10}$ or $UO_3{\cdot}2H_2O$) was formed at pH ~6.0, which could be further reduced to form $UO_2$(s) (Fig. 5A). This indicated that although U(VI) was partly precipitated under high pH conditions, all U(VI) species could be reduced to $UO_2$ by $MCN_{1.0}$ via photocatalysis [13].

The aforementioned results were further supported by the morphology observation. At pH ~5.0, no distinct change on $MCN_{1.0}$ was observed after U(VI) sorption. While after light irradiation, nanosized particles formed on the surface of $MCN_{1.0}$ (Fig. 6A). The interference fringe from the HRTEM image (Fig. 6B) showed a spacing of 0.310 nm, which is in accordance with the interplanar distance of the (1 1 1) plane of the $UO_2$ standard (0.315 nm, 00–041-1422-ICDD) [59]. Under high pH (6.0) conditions, needle-like meta-schoepite particles were formed on the $MCN_{1.0}$ surface (Fig. S12). These needle-like minerals gradually vanished after visible light irradiation, and $UO_2$ nanoparticles were formed on the $MCN_{1.0}$ surface (Fig. S12E and S12F).

Fig. 5B shows the U 4f spectra of U(VI)-accumulated $MCN_{1.0}$ before and after irradiation. Before irradiation, U $4f_{7/2}$ and U $4f_{5/2}$ peaks of the U(VI)-adsorbed $MCN_{1.0}$ surface were centered at 381.7 and 392.9 eV, respectively. However, the B.E. of U 4f shifted lower after visible light irradiation. U 4f signal can be quantitatively divided into two components, ascribing to the characteristics of U(VI) (at ~380.9 and ~391.8 eV) and U(IV) (at ~380.0 and ~390.9 eV) species, respectively [13]. According to the XPS analyses, 41.7% of U(IV) and 58.3% of U (VI) were detected, and the peak position of U(VI) displayed a significant shift compared to $UO_2^{2+}$ (Fig. 5B), possibly due to the surface re-oxidation of the generated $UO_2$ by photo-hole or oxyhydrogen radicals [13]. Therefore, X-ray absorption fine structure (XAFS) technique was further applied to determine the species of deposited uranium. Fig. 5C shows the U $L_{III}$-edge XANES of the uranium standard ($UO_2^{2+}$, $UO_2$(s), $U_3O_8$(s)) and uranium-loaded $MCN_{1.0}$ after irradiation. Obviously, the absorption edges of standard $UO_2$(s) and $U_3O_8$(s) shifted to lower energies compared to $UO_2^{2+}$. In U $L_{III}$-absorption, the near edges and shape of the uranium-loaded $MCN_{1.0}$ after irradiation showed perfect agreement with the $UO_2$ standard (Fig. 5C), which confirmed the predominant U(IV) species. Fig. 5D and 5E show the $k^3$-weighted

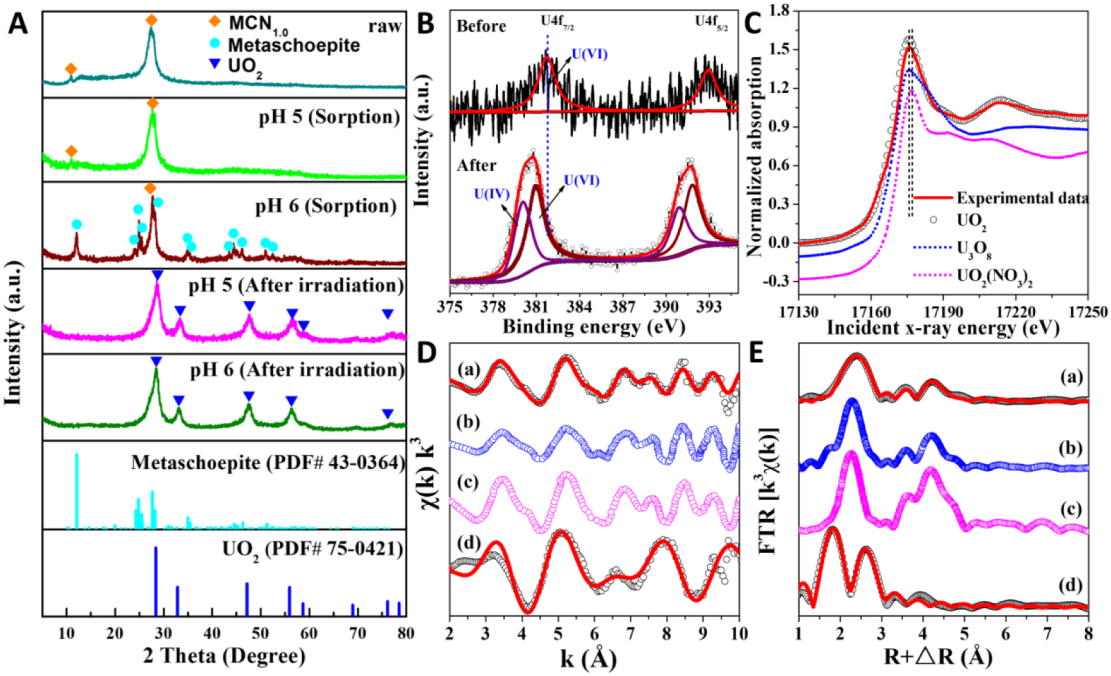


**Fig. 5.** XRD patterns of $MCN_{1.0}$ before and after photoreduction with $5.0 \times 10^{-4}$ mol/L U(VI) at pH 5.0 and 6.0 (A); XPS spectra of U 4f before and after irradiation (B); The U $L_{III}$-edge XANES spectra of U(VI)-loaded $MCN_{1.0}$ after irradiation (C); Uranium $L_{III}$-edge $k^3$-weighted EXAFS spectra (D) and the corresponding FTs (E) for the reference samples and U(VI)-reacted $MCN_{1.0}$ (a: U(VI) reacted $MCN_{1.0}$; b: Nano-uraninite standard (Data from Fletcher et al. [60]); c: $UO_2$ standard (Data from Fletcher et al. [60]); d: $UO_2^{2+}$ standard).

$\chi(k)$ function and corresponding Fourier transforms (FTs) of the standards ($UO_2$(s) and $UO_2^{2+}$), as well as the U-loaded $MCN_{1.0}$ samples after irradiation. After visible light irradiation, the $k^3\chi(k)$ function exhibited similar oscillation features to that of reference $UO_2$. The fitting results are tabulated in Table 2. For the typical structure of uranyl, the spectral fits lead to ~2.0 $O_{ax}$ (axial oxygen atom) at 1.8 Å and ~5.9 $O_{eq}$ (equator oxygen atom) at 2.5 Å, which are in agreement with the distances reported for other uranyl aqueous species [43,60,61]. While after irradiation, the central U atom was surrounded by ~6.1O atoms at $R$ ~2.4 Å and ~14.4O atoms at $R$ ~4.5 Å, as well as ~3.1 U atoms at $R$ ~3.9 Å, respectively, which are ascribed to the near-neighbor U-$O_1$ shell (the first oxygen shell), U-U shell, and outer U-$O_2$ shell (the second oxygen shell) of $UO_2$ (Table 2) [60,61]. The result indicated that the phase of $UO_2$(s) was formed after visible light irradiation. In addition, EXAFS fits clearly showed an additional coordination shell at ~2.1 Å with $CN$ ~2.5 O atoms in the first shell. Clearly, it was not the U-O interatomic distance from $UO_2$ or $UO_2^{2+}$ but may arise from other uranium oxides owing to the re-oxidization of $UO_2$ surface, in accordance with XPS results. Apparently, the detected species was document as $UO_2$ in EXAFS, which is significantly higher than that in XPS (41.7% U(IV)). The difference in the detected $U^{4+}$ content may be mainly caused by the difference in accuracy between XPS and EXAFS

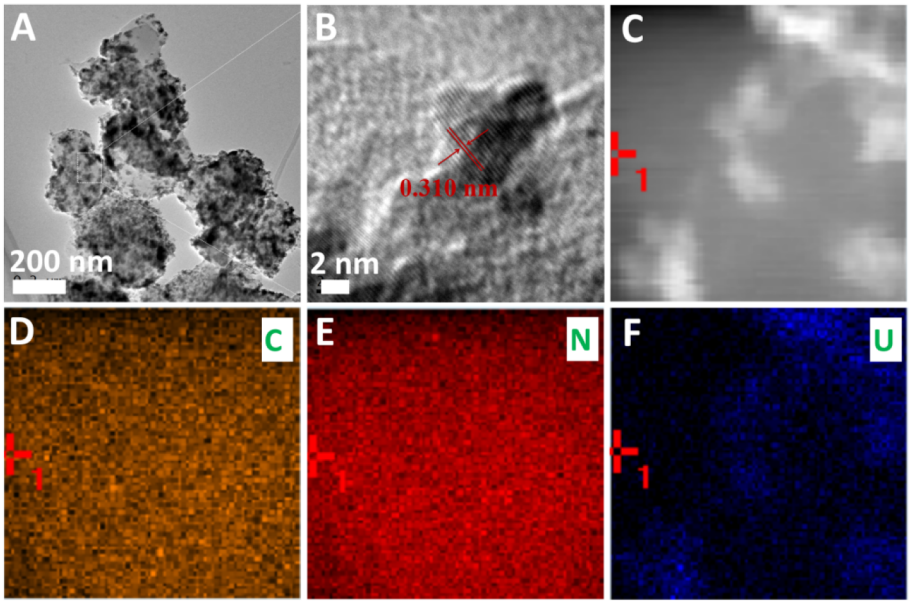


**Fig. 6.** TEM images of U(IV) deposition on $MCN_{1.0}$ (A); HRTEM of U(IV) deposition on $MCN_{1.0}$ (B) and Corresponding FFT image (inset); The image of U(IV) deposition on $MCN_{1.0}$ (C); Elemental distribution maps of C (D), N (E), and U (F) after irradiation. $C(UO_2^{2+}) = 5.0 \times 10^{-4}$ mol/L, pH = 6.0.

**Table 2**
Numerical results from modeling of the EXAFS data from the standards and the uranium-loaded $MCN_{1.0}$ samples.

| Samples | shells | CN | *R* (Å) | $\sigma^2$ | R-factor (%) |
|---|---|---|---|---|---|
| $UO_2^{2+}$ standard | U-$O_{ax}$ | 2.0 | 1.8 | 0.002 | 2.0 |
| | U-$O_{eq}$ | 5.9 | 2.5 | 0.008 | |
| $UO_2$ standard | U-O | 8.0 | 2.3 | 0.011 | 1.9 |
| | U-U | 12.0 | 3.9 | 0.006 | |
| | U-$O_2$ | 24.0 | 4.5 | 0.007 | |
| Nano-uraninite standard | U-O | 8.0 | 2.3 | 0.014 | 2.6 |
| | U-U | 4.2 | 3.8 | 0.006 | |
| | U-$O_2$ | 2.2 | 4.0 | 0.007 | |
| $MCN_{1.0}$-Uranium | U-O | 2.5 | 2.1 | 0.015 | 1.7 |
| | U-$O_1$ | 6.1 | 2.4 | 0.015 | |
| | U-U | 3.1 | 3.9 | 0.005 | |
| | U-$O_2$ | 14.4 | 4.5 | 0.012 | |

*Note*: R, bond distance; CN, coordination number; $\sigma^2$, Debye-Waller factor. The standard data of $UO_2$ and nano-uraninite ($U^{IV}O_2$(s)) were derived from Fletcher et al. [60].

(XPS technique only characterizes the top layer within 10 nm of the samples, while EXAFS could record the bulk information of the samples) [13,62].

The effect of holes and radicals on U(VI) photocatalytic reduction over $MCN_r$ were examined to further elucidate the reaction mechanism. ESR spin-trap experiment was carried out to detect the generation of free radicals ($^{\cdot}OH$ and $^{\cdot}O_2^-$) in $MCN_{1.0}$ system under visible light condition. As shown in Fig. 7A, there was no ESR signal when the reaction was performed in the dark. While under visible light irradiation, the characteristic peaks of DMPO-$^{\cdot}O_2^-$ and DMPO-$^{\cdot}OH$ (1:2:2:1 quartet pattern) adducts could be observed [63], and the intensity gradually increased with the irradiation time. These results indicated that $^{\cdot}O_2^-$ and $^{\cdot}OH$ indeed formed during the photocatalytic process. To test the efforts of these radicals on the photocatalytic reduction of U(VI), quenching experiments were further conducted. TBA (100 mmol/L), P-BQ (1 mmol/L) and methanol ($V(CH_3OH/H_2O)$ = 1:30) were added as scavengers for $^{\cdot}OH$ radicals, $^{\cdot}O_2^-$ radicals and holes, respectively. From Fig. 7B, methanol could act as hole trap for enhancing the separation of photoinduced electrons and holes, thus to enhance the photocatalytic reduction of U(VI). Moreover, during methanol oxidization process, reductive free radicals ($^{\cdot}CO_2^-$) might be produced to contribute to the reduction of U(VI) [64] (eqns. (3) and (4)). P-BQ could remarkably inhibited U(VI) removal, demonstrating the generated $^{\cdot}O_2^-$ radicals in the system $MCN_r$/U(VI)/visible light was also conductive to the photocatalytic reduction of U(VI) [57,65]. While the presence of TBA have slight influence on the U(VI) reduction, indicating that $^{\cdot}OH$ radicals played a negligible role in the reaction process. The above results confirmed that both photoinduced electrons and $^{\cdot}O_2^-$ radicals were involved in the photocatalytic reduction of U(VI).

In summary, the photocatalytic reduction process is illustrated as follows. Under visible light irradiation, U(VI) was reduced to form $UO_2$ deposits by photogenerated electron and $^{\cdot}O_2^-$. For the formed meta-schoepite particles under high pH conditions, there are two possible transformation mechanisms. One is that the meta-schoepite precipitates on the surface directly obtained photo-electrons or $^{\cdot}O_2^-$ to form $UO_2$. The other is that upon light irradiation, soluble U(VI) was converted to $UO_2$ on solid surface, breaking the chemical equilibrium between meta-schoepite precipitates and soluble U(VI). With the decrease in soluble U (VI), meta-schoepite gradually re-dissolved into solution, and further reduced to form $UO_2$. The proposed processes for the photocatalytic reduction of U(VI) to U(IV) is exhibited via Eqs. (2)–(12):

$$MCN + h\nu \rightarrow e_{(MCN)}^- + h_{(MCN)}^+ \text{ (excitation)} \quad (2)$$

$$CH_3OH + 6OH^- + 6h^+ \rightarrow CO_2 + 5H_2O \quad (3)$$

$$CH_3OH + OH^- + 4h^+ \rightarrow {}^{\cdot}CO_2^- + 5H^+ \quad (4)$$

$$O_2 + e^- \rightarrow {}^{\cdot}O_2^- \quad (5)$$

For soluble $UO_2^{2+}$:

$$UO_2^{2+} + 2e^- \rightarrow UO_2(s) \quad (6)$$

$$UO_2^{2+} + 2{}^{\cdot}O_2^- \rightarrow UO_2(s) + 2O_2 \quad (7)$$

For formed $UO_3{\cdot}2H_2O$ precipitates, two ways are presumed:

$$UO_3{\cdot}2H_2O + 2H^+ + 6e^- \rightarrow UO_2(s) + 3H_2O \quad (8)$$

$$UO_3{\cdot}2H_2O + 2H^+ + 2{}^{\cdot}O_2^- \rightarrow UO_2(s) + 2O_2 + 3H_2O \quad (9)$$

or

$$UO_3{\cdot}2H_2O \rightarrow UO_2^{2+} + H_2O + 2OH^- \quad (10)$$

$$UO_2^{2+} + 2e^- \rightarrow UO_2(s) \quad (11)$$

$$UO_2^{2+} + 2{}^{\cdot}O_2^- \rightarrow UO_2(s) + 2O_2 \quad (12)$$

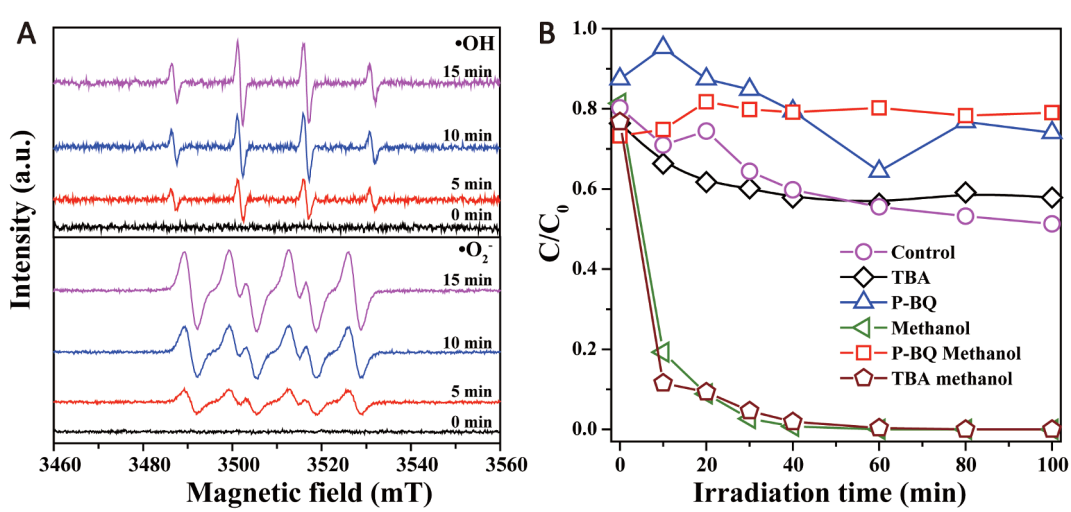


**Fig. 7.** ESR spectra of radical adducts trapped by DMPO ($^{\cdot}O_2^-$ and $^{\cdot}OH$) in $MCN_{1.0}$ dispersion in the dark and with the visible light irradiation for 5 min, 10 min and 15 min (A); The photocatalytic reduction plots of U(VI) over $MCN_{1.0}$ with the addition of hole, $^{\cdot}O_2^-$ and $^{\cdot}OH$ radical scavenger under visible light irradiation (B), Note: only U(VI) and $MCN_{1.0}$ were contained in the control group.

## 4. Conclusions

Mesoporous g-$C_3N_4$ was fabricated for the photocatalytic reduction of U(VI) under visible light. Owing to the introduction of adjustable meso-holes, $MCN_r$ provided a high surface-to-volume ratio, appropriate surface deficiency, and enhanced visible light absorption. $MCN_{1.0}$ possessed the highest surface area (191 $m^2$/g, increased by 21.8 fold) and largest pore volumes (52.1 $cm^3$/g, increased by 13 fold), exhibiting the highest performance for photocatalytic U(VI) reduction (6.75 fold higher than BCN). A high extraction capacity of uranium (2.99 g/g) was achieved over light illuminated $MCN_{1.0}$. In the presence of co-existing ions, $MCN_{1.0}$ exhibited relatively high selectivity for the photo-reduction of U(VI). The deposited uranium on $MCN_{1.0}$ could be efficiently recovered simply by exposure in air for 24 h, and further eluted with a 0.1 mol/L $Na_2CO_3$ solution. Moreover, $MCN_r$ could maintain stable during the photocatalytic reactions. XRD and TEM confirmed that U(VI) was converted to $UO_2$(s) phase on the $MCN_r$ surface during photocatalysis, while XPS, XANES, and EXAFS further confirmed that the formed $UO_2$(s) on $MCN_r$ surface was partly re-oxidized by radicals and holes. However, the process of re-oxidation of $UO_2$(s) did not lead a dissolution of deposited uranium, and thus, exerted no obvious influence on the extraction efficiency of U(VI). Above all, $MCN_r$ here represent potentially a simple and cost-effective photocatalytic materials, showing clear advantages over traditional uranium sorbent materials. This strategy can provide guidance toward efficient, economic, and applicable treatment of uranium from water.

## Acknowledgements

Financial supports from National Natural Science Foundation of China (21601169, 21601179, 41573128, 21876172, and U1732132), Natural Science Foundation of Gansu Province (17JR5RA309), the "100-Talent" program from Chinese Academy of Sciences, CAS "Light of West China" Program, and the Key Laboratory Project of Gansu Province (Grant No. 1309RTSA041).

## Conflicts of interest statement

The authors declare no competing financial interests.

## Appendix A. Supplementary data

Supplementary data to this article can be found online at https://doi.org/10.1016/j.cej.2019.123193.

## References

[1] C. Liu, P.C. Hsu, J. Xie, J. Zhao, T. Wu, H.T. Wang, W. Liu, J.S. Zhang, S. Chu, Y. Cui, A half-wave rectified alternating current electrochemical method for uranium extraction from seawater, Nat. Energy 44 (2017) 17007.
[2] C. Tsouris, Uranium extraction: fuel from seawater, Nat. Energy 2 (2017) 17022.
[3] S. Lee, U. Kang, G. Piao, S. Kim, D.S. Han, H. Park, Homogeneous photoconversion of seawater uranium using copper and iron mixed-oxide semiconductor electrodes, Appl. Catal. B: Environ. 207 (2017) 35–41.
[4] X.X. Wang, L. Chen, Lin Wang, Q.H. Fan, D.Q. Pan, J.X. Li, F.T. Chi, Y. Xie, S.J. Yu, C.L. Xiao, F. Luo, J. Wang, X.L. Wang, C.L. Chen, W.S. Wu, W.Q. Shi, S.A. Wang, X.K. Wang, Synthesis of novel nanomaterials and their application in efficient removal of radionuclides, Sci. China: Chem. 62 (2019) 933–967.
[5] X. Xu, H.J. Zhang, J.X. Ao, L. Xu, X.Y. Liu, X.J. Guo, J.Y. Li, L. Zhang, Q.N. Li, X.Y. Zhao, B.J. Ye, D.L. Wang, F. Shen, H.J. Ma, 3D hierarchical porous amidoxime fibers speed up uranium extraction from seawater, Energy Environ. Sci. 12 (2019) 1979–1988.
[6] C.X. Ma, J.X. Gao, D. Wang, Y.H. Yuan, J. Wen, B.J. Yan, S.L. Zhao, X.M. Zhao, Y. Sun, X.L. Wang, N. Wang, Sunlight polymerization of poly(amidoxime) hydrogel membrane for enhanced uranium extraction from seawater, Adv. Sci. 6 (2019) 1900085.
[7] Q.H. Yu, Y.H. Yuan, J. Wen, X.M. Zhao, S.L. Zhao, D. Wang, C.Y. Li, X.L. Wang, N. Wang, A universally applicable strategy for construction of anti-biofouling adsorbents for enhanced uranium recovery from seawater, Adv. Sci. 6 (2019) 1900002.
[8] W. Luo, G. Xiao, F. Tian, J.J. Richardson, Y.P. Wang, J.F. Zhou, J.L. Guo, X.P. Liao, B. Shi, Engineering robust metal-phenolic network membranes for uranium extraction from seawater, Energy Environ. Sci. 12 (2019) 607–614.
[9] Q. Sun, B. Aguila, J. Perman, A.S. Ivanov, V.S. Bryantsev, L.D. Earl, C.W. Abney, L. Wojtas, S.Q. Ma, Bio-inspired nano-traps for uranium extraction from seawater and recovery from nuclear waste, Nat. Commun. 9 (2018) 1644.
[10] C.W. Abney, R.T. Mayes, T. Saito, S. Dai, Materials for the recovery of uranium from seawater, Chem. Rev. 117 (2017) 13935–14013.
[11] J. Kim, C. Tsouris, R.T. Mayes, Y. Oyola, T. Saito, C.J. Janke, S. Dai, E. Schneider, D. Sachde, Recovery of uranium from seawater: A review of current status and future research needs, Sep. Sci. Technol. 48 (2013) 367–387.
[12] M.Y. Xu, X.L. Han, D.B. Hua, Polyoxime-functionalized magnetic nanoparticles for uranium adsorption with high selectivity over vanadium, J. Mater. Chem. A 5 (2017) 12278–12284.
[13] P. Li, J.J. Wang, Y. Wang, J.J. Liang, B.H. He, D.Q. Pan, Q.H. Fan, X.K. Wang, Photoconversion of U(VI) by $TiO_2$: an efficient strategy for seawater uranium extraction, Chem. Eng. J. 365 (2019) 231–241.
[14] P. Li, J.J. Wang, T. Peng, Y. Wang, J.J. Liang, D.Q. Pan, Q.H. Fan, Heterostructure of anatase-rutile aggregates boosting the photoreduction of U(VI), Appl. Surf. Sci. 483 (2019) 670–676.
[15] P. Li, J.J. Wang, Y. Wang, J.J. Liang, D.Q. Pan, S.R. Qiang, Q.H. Fan, An overview and recent progress in the heterogeneous photocatalytic reduction of U(VI), J. Photochem. Photobiol. C 41 (2019) 100320.
[16] S. Garcia-Segura, E. Brillas, Applied photoelectrocatalysis on the degradation of organic pollutants in wastewaters, J. Photochem. Photobiol. C 31 (2017) 1–35.
[17] L.Y. Ozer, C. Garlisi, H. Oladipo, M. Pagliaro, S.A. Sharief, A. Yusuf, S. Almheiri, G. Palmisano, Inorganic semiconductors-graphene composites in photo (electro) catalysis: synthetic strategies, interaction mechanisms and applications, J. Photochem. Photobiol. C 33 (2017) 132–164.
[18] Z. Li, X. Meng, Z. Zhang, Recent development on $MoS_2$-based photocatalysis: a review, J. Photochem. Photobiol. C 35 (2018) 39–55.
[19] K. Vikrant, C.M. Park, K. Kim, S. Kumar, E. Jeon, Recent advancements in photocatalyst-based platforms for the destruction of gaseous benzene: performance evaluation of different modes of photocatalytic operations and against adsorption techniques, J. Photochem. Photobiol. C 41 (2019) 100316.
[20] H. Li, F.W. Zhai, D.X. Gui, X.X. Wang, C.F. Wu, D. Zhang, X. Dai, H. Deng, X.T. Su, J. Diwu, Z. Lin, Z.F. Chai, S.A. Wang, Powerful uranium extraction strategy with combined ligand complexation and photocatalytic reduction by postsynthetically modified photoactive metal-organic frameworks, Appl. Catal. B: Environ. 254 (2019) 47–54.
[21] Y. Li, G. Zou, S.Y. Yang, Z.H. Wang, T. Chen, X.F. Yu, Q. Guo, R. He, T. Duan, W.K. Zhu, Integration of bio-inspired adsorption and photodegradation for the treatment of organics-containing radioactive wastewater, Chem. Eng. J. 364 (2019) 139–145.
[22] H.H. Wang, H. Guo, N. Zhang, Z.S. Chen, B.W. Hu, X.K. Wang, Enhanced Photoreduction of U(VI) on $C_3N_4$ by Cr(VI) and Bisphenol A: ESR, XPS and EXAFS Investigation, Environ. Sci. Technol. 53 (2019) 6454–6461.
[23] Z.J. Li, Z.W. Huang, W.L. Guo, L. Wang, L.R. Zheng, Z.F. Cha, W.Q. Shi, Enhanced photocatalytic removal of uranium(VI) from aqueous solution by magnetic $TiO_2$/$Fe_3O_4$ and its graphene composite, Environ. Sci. Technol. 51 (2017) 5666–5674.
[24] C.H. Lu, P. Zhang, S.J. Jiang, X. Wu, S.Q. Song, M.S. Zhu, Z.Z. Lou, Z. Li, F. Liu, Y.H. Liu, Y. Wang, Z.G. Le, Photocatalytic reduction elimination of $UO_2^{2+}$ pollutant under visible light with metal-free sulfur doped g-$C_3N_4$ photocatalyst, Appl. Catal. B: Environ. 200 (2017) 378–385.
[25] C.H. Lu, R.Y. Chen, X. Wu, M.F. Fan, Y.H. Liu, A.G. Le, S.J. Jiang, S.Q. Song, Boron doped g-$C_3N_4$ with enhanced photocatalytic $UO_2^{2+}$ reduction performance, Appl. Surf. Sci. 360 (2016) 1016–1022.
[26] M.D. Hernandez-Alonso, F. Fresno, S. Suarez, J.M. Coronado, Development of alternative photocatalysts to $TiO_2$: challenges and opportunities, Energy Environ. Sci. 2 (2009) 1231–1257.
[27] X.C. Wang, K. Maeda, A. Thomas, K. Takanabe, G. Xin, J.M. Carlsson, K. Domen, M. Antonietti, A metal-free polymeric photocatalyst for hydrogen production from water under visible light, Nat. Mater. 8 (2009) 76–80.
[28] F. Ding, D. Yang, Z.W. Tong, Y.H. Nan, Y.J. Wang, X.Y. Zou, Z.Y. Jiang, Graphitic carbon nitride-based nanocomposites as visible-light driven photocatalysts for environmental purification, Environ. Sci.: Nano 4 (2017) 1455–1469.
[29] Y. Zheng, J. Liu, J. Liang, M. Jaroniec, S.Z. Qiao, Graphitic carbon nitride materials: controllable synthesis and applications in fuel cells and photocatalysis, Energy Environ. Sci. 5 (2012) 6717–6731.
[30] A. Mishra, A. Mehta, S. Basu, N.P. Shetti, K.R. Reddy, T.M. Aminabhavi, Graphitic carbon nitride (g-$C_3N_4$)-based metal-free photocatalysts for water splitting: a review, Carbon 149 (2019) 693–721.
[31] W.J. Ong, L.L. Tan, Y.H. Ng, S.T. Yong, S.P. Chai, Graphitic carbon nitride (g-$C_3N_4$)-based photocatalysts for artificial photosynthesis and environmental remediation: Are we a step closer to achieving sustainability? Chem. Rev. 116 (2016) 7159–7329.
[32] J.Q. Wen, J. Xie, X.B. Chen, X. Li, A review on g-$C_3N_4$-based photocatalysts, Appl. Surf. Sci. 391 (2017) 72–123.
[33] G.P. Dong, Y.H. Zhang, Q.W. Pan, J.R. Qiu, A fantastic graphitic carbon nitride (g-$C_3N_4$) material: electronic structure, photocatalytic and photoelectronic properties, J. Photochem. Photobiol., C 20 (2014) 33–50.
[34] S. Ye, R. Wang, M.Z. Wu, Y.P. Yuan, A review on g-$C_3N_4$ for photocatalytic water splitting and $CO_2$ reduction, Appl. Surf. Sci. 358 (2015) 15–27.
[35] Z. Yao, J. Liu, J. Liang, M. Jaroniec, S.Z. Qiao, Graphitic carbon nitride materials: controllable synthesis and applications in fuel cells and photocatalysis, Energy Environ. Sci. 5 (2012) 6717–6731.
[36] Y. Wang, X.C. Wang, M. Antonietti, Polymeric graphitic carbon nitride as a

heterogeneous organocatalyst: From photochemistry to multipurpose catalysis to sustainable chemistry, Angew. Chem. Int. Ed. 51 (2012) 68–89.
[37] J. Xu, H.T. Wu, X. Wang, B. Xue, Y.X. Li, Y. Cao, A new and environmentally benign precursor for the synthesis of mesoporous g-$C_3N_4$ with tunable surface area, Phys. Chem. Chem. Phys. 15 (2013) 4510–4517.
[38] X.F. Chen, Y.S. Jun, K. Takanabe, K. Maeda, K. Domen, X.Z. Fu, M. Antonietti, X.C. Wang, Ordered mesoporous SBA-15 type graphitic carbon nitride: a semiconductor host structure for photocatalytic hydrogen evolution with visible light, Chem. Mater. 21 (2009) 4093–4095.
[39] Q. Li, J.P. Yang, D. Feng, Z.X. Wu, Q.L. Wu, S.S. Park, C.S. Ha, D.Y. Zhao, Facile synthesis of porous carbon nitride spheres with hierarchical three-dimensional mesostructures for $CO_2$ capture, Nano Res. 3 (2010) 632–642.
[40] A. Vinu, Two-dimensional hexagonally-ordered mesoporous carbon nitrides with tunable pore diameter, surface area and nitrogen content, Adv. Funct. Mater. 18 (2008) 816–827.
[41] F. Goettmann, A. Fischer, M. Antonietti, A. Thomas, Chemical synthesis of mesoporous carbon nitrides using hard templates and their use as a metal-free catalyst for friedel-crafts reaction of benzene, Angew. Chem. Int. Ed. 45 (2006) 4467–4471.
[42] Y.J. Yang, D.W. Ni, Y. Yao, Y.T. Zhong, Y. Ma, J.N. Yao, High photocatalytic activity of carbon doped $TiO_2$ prepared by fast combustion of organic capping ligands, RSC Adv. 5 (2015) 93635–93643.
[43] Z.W. Niu, X.Y. Wei, S.R. Qiang, H.Y. Wu, D.Q. Pan, W.S. Wu, Q.H. Fan, Spectroscopic studies on U(VI) incorporation into $CaCO_3$: Effects of aging time and U(VI) concentration, Chemosphere 220 (2019) 1100–1107.
[44] B. Ravel, M. Newville, ARTEMIS, HEPHAESTUS: data analysis for X-ray absorption spectroscopy using IFEFFIT, J. Synchrotron Rad. 12 (2005) 537–541.
[45] S.I. Zabinsky, J.J. Rehr, A. Ankudinov, R.C. Albers, M.J. Eller, Multiple-scattering calculations of x-ray-absorption spectra, Phys. Rev. B 52 (1995) 2995–3009.
[46] S.Y. Tan, Z.P. Xing, J.Q. Zhang, Z.Z. Li, X.Y. Wu, J.Y. Cui, J.Y. Kuang, J.W. Yin, W. Zhou, Meso-g-$C_3N_4$/g-$C_3N_4$ nanosheets laminated homojunctions as efficient visible-light-driven photocatalysts, Int. J. Hydrogen Energy 42 (2017) 25969–25979.
[47] Q.H. Liang, Z. Li, Z.H. Huang, F.Y. Kang, Q.H. Yang, Holey graphitic carbon nitride nanosheets with carbon vacancies for highly improved photocatalytic hydrogen production, Adv. Funct. Mater. 25 (2015) 6885–6892.
[48] S.W. Cao, J.X. Low, J.G. Yu, M. Jaroniec, Polymeric photocatalysts based on graphitic carbon nitride, Adv. Mater. 27 (2015) 2150–2176.
[49] P.J. Yang, H.Y. Zhuzhang, R.R. Wang, W. Lin, X.C. Wang, Carbon vacancies in a melon polymeric matrix promote photocatalytic carbon dioxide conversion, Angew. Chem. Int. Ed. 58 (2019) 1134–1137.
[50] X.D. Zhang, X. Xie, H. Wang, J.J. Zhang, B.C. Pan, Y. Xie, Enhanced Photoresponsive Ultrathin Graphitic-Phase $C_3N_4$ Nanosheets for Bioimaging, J. Am. Chem. Soc. 135 (2013) 18–21.
[51] N. Tian, H.W. Huang, Y. He, Y.X. Guo, T.R. Zhang, Y.H. Zhang, Mediator-free direct Z-scheme photocatalytic system: $BiVO_4$/g-$C_3N_4$ organic-inorganic hybrid photocatalyst with highly efficient visible-light-induced photocatalytic activity, Dalton Trans. 44 (2015) 4297–4307.
[52] V.N. Salomone, J.M. Meichtry, G. Zampieri, M.I. Litter, New insights in the heterogeneous photocatalytic removal of U(VI) in aqueous solution in the presence of 2-propanol, Chem. Eng. J. 261 (2015) 27–35.
[53] P. Niu, L.L. Zhang, G. Liu, H.M. Cheng, Graphene-like carbon nitride nanosheets for improved photocatalytic activities, Adv. Funct. Mater. 22 (2012) 4763–4770.
[54] L. Chen, Z.L. Bai, L. Zhu, L.J. Zhang, Y.W. Cai, Y.X. Li, W. Liu, Y.L. Wang, L.H. Chen, D.W. Juan, J.Q. Wang, Z.F. Chai, S. Wang, Ultrafast and efficient extraction of uranium from seawater using an amidoxime appended metal-organic framework, ACS Appl. Mater. Interfaces 9 (2017) 32446–32451.
[55] U.K. Saha, S. Taniguchi, K. Sakurai, Simultaneous adsorption of cadmium, zinc, and lead on hydroxyaluminum- and hydroxyaluminosilicate- montmorillonite complexes, Soil Sci. Soc. Am. J. 66 (2002) 117–128.
[56] P. Amadelli, A. Maldotti, S. Sostero, V. Carassiti, Photodeposition of uranium oxides onto $TiO_2$ from aqueous uranyl solutions, J. Chem. Soc. Faraday Trans. 87 (1991) 3267–3273.
[57] Y.K. Kim, S. Lee, J. Ryu, H. Park, Solar conversion of seawater uranium(VI) using $TiO_2$ electrodes, Appl. Catal. B: Environ. 163 (2015) 584–590.
[58] M. Bonato, G.C. Allen, T.B. Scott, Reduction of U(VI) to U(IV) on the surface of $TiO_2$ anatase nanotubes, Micro Nano Lett. 3 (2008) 57–61.
[59] J.C. Xie, J.F. Lin, X.H. Zhou, pH-dependent microbial reduction of uranium(VI) in carbonate-free solutions: UV-vis, XPS, TEM, and thermodynamic studies, Environ. Sci. Pollut. Res. 25 (2018) 22308–22317.
[60] K.E. Fletcher, M.I. Boyanov, S.H. Thomas, Q.Z. Wu, K.M. Kemner, F.E. Loffler, U(VI) reduction to mononuclear U(IV) by desulfitobacterium species, Environ. Sci. Technol. 44 (2010) 4705–4709.
[61] G.D. Sheng, P.J. Yang, Y.N. Tang, Q.Y. Hu, H. Li, X.M. Ren, B.W. Hu, X.K. Wang, Y.Y. Huang, New insights into the primary roles of diatomite in the enhanced sequestration of $UO_2^{2+}$ by zerovalent iron nanoparticles: An advanced approach utilizing XPS and EXAFS, Appl. Catal. B: Environ. 193 (2016) 189–197.
[62] S. Hoang, S.P. Berglund, N.T. Hahn, A.J. Bard, C.B. Mullins, Enhancing visible light photo-oxidation of water with $TiO_2$ nanowire arrays via cotreatment with $H_2$ and $NH_3$: Synergistic effects between $Ti^{3+}$ and N, J. Am. Chem. Soc. 134 (2012) 3659–3662.
[63] Y.C. Deng, L. Tang, C.Y. Feng, G.M. Zeng, J.J. Wang, Y.Y. Zhou, Y.N. Liu, B. Peng, H.P. Feng, Construction of plasmonic Ag modified phosphorous-doped ultrathin g-$C_3N_4$ nanosheets/$BiVO_4$ photocatalyst with enhanced visible-near-infrared response ability for ciprofloxacin degradation, J. Hazard. Mater. 344 (2018) 758–769.
[64] Y.D. Guo, L. Ling, Y.R. Li, Z.B. Li, X.G. Wang, G.H. Wang, Adsorption and photocatalytic reduction activity of uranium(VI) on zinc oxide/rectorite composite enhanced with methanol as sacrificial organics, J. Radioanal. Nucl. Chem. 310 (2016) 883–890.
[65] L. Hu, X.W. Yan, X.J. Zhang, D. Shan, Integration of adsorption and reduction for uranium uptake based on $SrTiO_3$/$TiO_2$ electrospun nanofibers, Appl. Surf. Sci. 428 (2018) 819–824.